ADVANCED FUNCTIONAL MATERIALS
www.afm-journal.de

# Amorphous High Entropy Alloy Nanosheets Enabling Robust Li–S Batteries

*Ren He, Seungho Lee, Yang Ding, Chen Huang, Xuan Lu, Lirong Zheng, Ao Yu, Chaoyue Zhang, Canhuang Li, Xiaoyu Bi, Yaqiang Li, Yaqi Liao, Junshan Li, Ahmad Ostovari Moghaddam, Salimov Yernar, Ying Xu, Maria Ibáñez, Chaoqi Zhang,* Linlin Yang,* Yingtang Zhou,* and Andreu Cabot**

**High-entropy alloys (HEAs) show great potential for catalyzing complex multi-step reactions, but optimizing their parameters, i.e., composition, but also their crystallinity and morphology, remains a significant challenge. In this study, FeCoNiMoW HEAs are synthesized into either amorphous nanosheets (HEANS) or crystalline nanoparticles (HEANP), which are then used to catalyze the lithium–sulfur (Li–S) reaction of Li–S batteries (LSBs). Evaluations in symmetric cells, coin cells, and pouch cells reveal that HEANS significantly enhance LSB performance, achieving initial discharge capacities up to 1632 mAh $g^{-1}$. The batteries also exhibit excellent cycling stability over 1000 cycles at 3Cand maintain high-rate performance up to 10C with a capacity of 614 mAh $g^{-1}$. Comprehensive in situ analyses and density functional theory calculations demonstrate that amorphous HEANS provide more active sites, better ionic conductivity and stronger chemical interactions with lithium polysulfides (LiPS). These properties effectively suppress the shuttle effect, promote the complete $S_8 \rightarrow Li_2S$ conversion by reducing the impedance of the solid-electrolyte interphase, and accelerate the $Li_2S_4 \rightarrow Li_2S_2$ step by lowering the nucleation energy barrier. Overall, this study highlights the superior catalytic properties of amorphous 2D HEAs in LSBs and offers new insights into the mechanisms of LiPS conversion.**

## 1. Introduction

Rechargeable lithium–sulfur (Li–S) batteries (LSBs) are a high-energy density alternative to conventional Li-ion batteries.[1] The Li–S conversion reaction at their cathode offers a potential energy density of 2600 Wh $kg^{-1}$ and a specific capacity of 1675 mAh $g^{-1}$. However, achieving full $S_8 \leftrightarrow Li_2S$ conversion during extended charge-discharge cycles remains a formidable challenge. The difficulty arises from the electrically insulating character of both solid sulfur and $Li_2S$, the sluggish Li–S redox kinetics, and the solubility of lithium polysulfide (LiPS) in the commonly used ether-based electrolytes.[2] These challenges are exacerbated by the high sulfur areal loadings needed for practical applications.

Due to the inherently complex nature of Li–S reactions, which involve multiple intermediate species and sequential chemical and redox steps,[3] maximizing

R. He, C. Huang, X. Lu, A. Yu, C. Zhang, X. Bi, L. Yang, A. Cabot
Catalonia Institute for Energy Research – IREC
Sant Adrià de Besòs, Barcelona 08930, Spain
E-mail: lyang@irec.cat; acabot@irec.cat

R. He, C. Huang, A. Yu, C. Li, X. Bi, L. Yang
Universitat de Barcelona
Barcelona 08028, Spain

S. Lee, M. Ibáñez
Institute of Science and Technology Austria (ISTA)
Am Campus 1, Klosterneuburg 3400, Austria

Y. Ding, Y. Xu
Hebei Key Lab of Optic-electronic Information and Materials
College of Physics Science and Technology
Hebei University
Baoding 071002, China

X. Lu
Universitat Politècnica de Catalunya
Campus Diagonal Sud, Edificio PC (Pavelló C). Av. Diagonal, 647,
Barcelona 08028, Spain

L. Zheng
Institute of High Energy Physics
Chinese Academy of Sciences
Beijing 100049, P. R. China

Y. Li, C. Zhang
Fuzhou University
Fuzhou, Fujian 350116, P. R. China
E-mail: chaoqizhang@fzu.edu.cn

Y. Liao
State Key Laboratory of Material Processing and Die and Mold Technology
School of Materials Science and Engineering
Huazhong University of Science and Technology
Wuhan 430074, P. R. China

The ORCID identification number(s) for the author(s) of this article can be found under https://doi.org/10.1002/adfm.202513859



**DOI: 10.1002/adfm.202513859**

their kinetics requires catalytic materials that offer diverse surface adsorption sites and tunable electronic energy levels.[4] These catalysts can be integrated either directly into the sulfur cathode or introduced at the cathode-facing side of the separator, i.e., at the electrolyte-cathode interphase, where the Li–S redox reactions primarily occur. The latter strategy allows for simplifying the cathode composition, thereby facilitating its optimization and reducing overall manufacturing costs.[5]

High-entropy alloys (HEAs), which incorporate five or more principal metals, emerge as ideal catalysts to accelerate the Li–S reaction in LSBs, thereby enhancing battery performance.[6] The heterogeneous nature of HEAs provides multiple surface elemental sites.[7] Besides, the differences in atomic radii and electronegativity among these elements lead to significant lattice distortions and defects,[8] which extend the range of electronic energy levels available on the material surface and create localized regions of charge accumulation and depletion that can be effective for trapping and converting LiPS, further facilitating the Li–S reaction.[9]

We have recently demonstrated the successful synthesis of FeCoNiMoW nanoparticles and their outstanding catalytic activity toward oxygen redox reactions.[8b] The choice of Fe, Co, and Ni is driven by their abundance, cost-effectiveness, and similar atomic radii, which together facilitate HEA nucleation. Mo and W are incorporated for their high electronegativity, which promotes strong adsorption of reaction intermediates. The synergistic interaction among 3d, 4d, and 5d transition metals in the alloy induces a redistribution of electron density and modifies the density of states near the Fermi level. This electronic tuning enhances the affinity of Mo and W for reactive species, stabilizing intermediates through stronger d-p orbital overlap with oxygen.[10]

However, several critical aspects remain unexplored. In particular, the kinetic control during the HEA formation process has yet to be systematically investigated, which could offer new insights into the nucleation and structural regulation of multimetallic systems. Beyond structural considerations, the strong d–p orbital overlap with sulfur renders HEAs promising candidates for catalyzing the Li–S redox reactions in LSBs, through enhanced interactions with LiPSs. Recent studies reflect a growing interest in high-entropy materials for LSB electrocatalysis. For instance, a high-entropy carbonitride MXene, featuring high mechanical strain and five distinct metal–nitrogen bonds, demonstrated excellent rate performance, achieving up to 4C capability in LSBs.[7a] Similarly, a PdSnNiCoCuP high-entropy phosphide employed as a sulfur host exhibited a high initial discharge capacity of 1059 mAh $g^{-1}$ at 0.1C.[11] Moreover, PtCuFeCoNi HEAs have been shown to effectively catalyze the stepwise conversion of LiPSs via abundant surface-active site.[12]

Beyond composition, understanding the influence of the HEA architecture on LSB performance is essential for guiding catalyst design. However, tuning the porosity, dimensionality, and crystallinity of HEAs presents significant challenges. At the nanoscale, surface and interphase energies contribute to stabilizing high entropy solid solutions.[13] However, kinetically, the complex and varying redox potential of different metal ions and disparities in elemental diffusion rates complicate the prediction and control of stable phases, which makes the understanding of their structural impact on LSB catalytic performance limited.

To bridge this gap, this study prospectively investigates the effects of HEA structure on LSB performance. Using a carbon monoxide surface confinement strategy, FeCoNiMoW HEAs with varying architecture and crystallinity, are synthesized. Specifically, amorphous FeCoNiMoW HEA nanosheets (HEANS) and crystalline HEA nanoparticles (HEANP) are produced and tested as catalyst at the separator or LSBs. The electrochemical performance of coin-type and pouch-type LSBs incorporating such HEA-modified separators is then evaluated under practical conditions. To gain deeper mechanistic insights, in situ Raman spectroscopy and electrochemical impedance spectroscopy (EIS), combined with galvanostatic intermittent titration technique (GITT) measurements and distribution of relaxation time (DRT) analyses, along with density functional theory (DFT) calculations, are employed to investigate diffusion impedance, reaction energy barriers, and adsorption energies at various stages of the LiPS conversion process. The findings reveal that amorphous HEANS outperform crystalline HEANPs in enhancing LSB performance, providing fundamental insights into the critical role of HEA structure in optimizing sulfur redox kinetics and stability. Overall, this study boosts a comprehensive understanding of structure-property relationships in HEAs, offering a rational design strategy for advancing next-generation LSB technology.

## 2. Results and Discussion

### 2.1. HEA Synthesis and Characterization

FeCoNiMoW HEA nanostructures were synthesized in solution by co-reduction of the different metal salt precursors at 260 °C (**Figure 1a**; Table S1, Supporting Information, see additional details in the Experimental Section of the Supporting Information, SI).[14] The thermal decomposition of $Mo(CO)_6$ and $W(CO)_6$ at 160–200 °C yields the respective zero-valent metals, while simultaneously releasing carbon monoxide (CO). The generated CO

J. Li
Institute of Advanced Study
Chengdu University
Chengdu 610106, P. R. China
A. Ostovari Moghaddam
Tikhonov Moscow Institute of Electronics and Mathematics
HSE University
Moscow 101000, Russia
S. Yernar
Al-Farabi Kazakh National University
Faculty of Physics and Technology
Department of Plasma Physics
Almaty 050040, Republic of Kazakhstan
Y. Zhou
Zhejiang Key Laboratory of Petrochemical Environmental Pollution Control
National Engineering Research Center for Marine Aquaculture
Marine Science and Technology College
Zhejiang Ocean University
Zhoushan, Zhejiang Province 316004, P. R. China
E-mail: zhouyingtang@zjou.edu.cn
A. Cabot
ICREA
Pg. Lluis Companys 23, Barcelona, Catalonia 08010, Spain

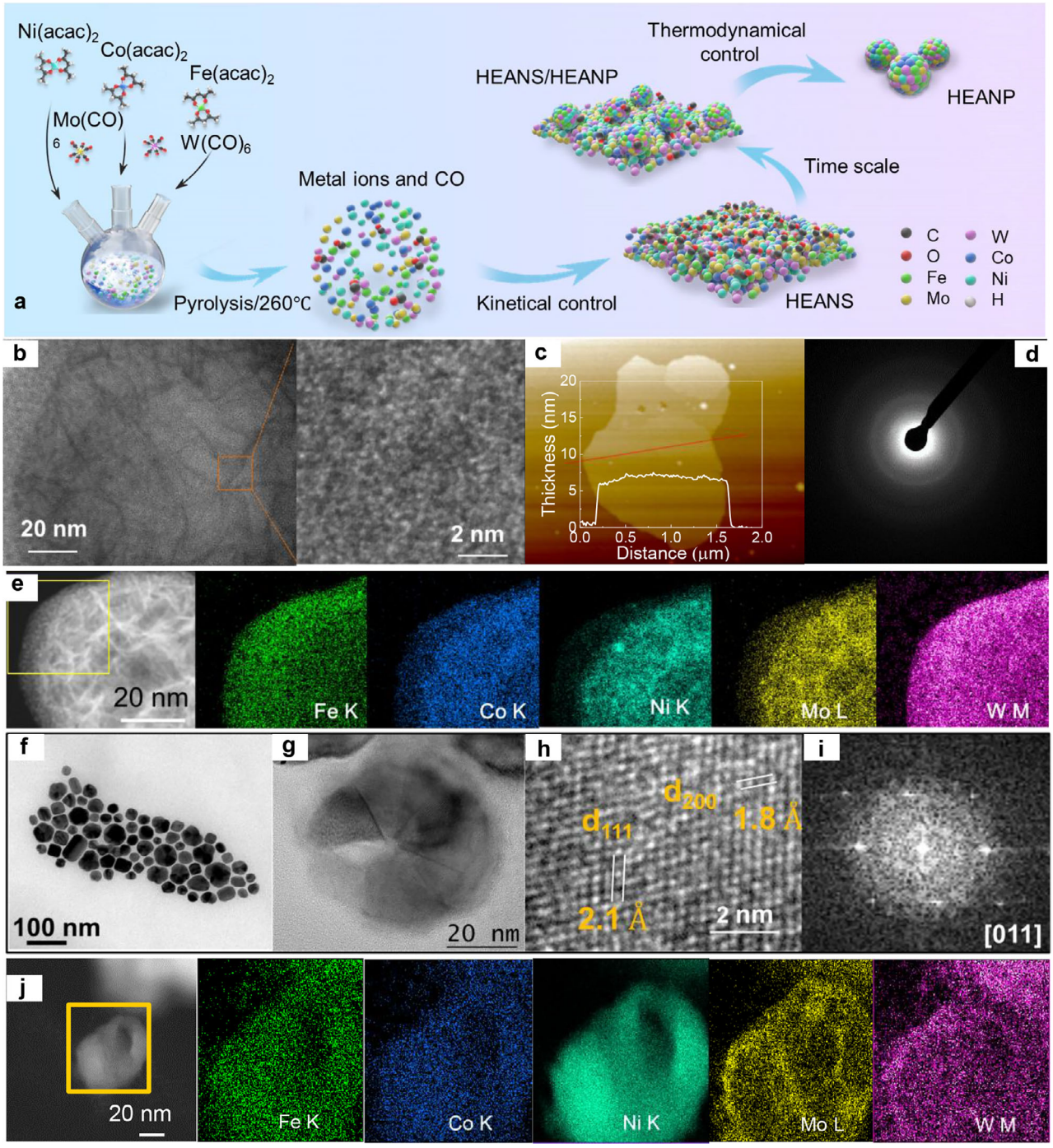


**Figure 1.** Synthesis procedure and structural and chemical characterization of FeCoNiMoW HEAs. a) Scheme of the FeCoNiMoW HEANS and HEANP synthesis process. b) TEM and HRTEM images, c) atomic-force microscopy image and thickness profile, d) electron diffraction pattern, e) HAADF-STEM micrograph and EDS compositional maps of amorphous FeCoNiMoW HEANSs. f,g) TEM images, h) HRTEM image, i) FFT pattern, j) HAADF-STEM micrograph and EDS compositional maps of crystalline FeCoNiMoW HEANPs.

plays a dual role: it assists in the reduction of the 3d metal ions and stabilizes the resulting nanostructures due to its strong binding affinity for low-index metal surfaces.[15] As a result of this reduction process, nanosheet (NS)-like structures, with an average thickness of 7 nm, were obtained after just 10 min of reaction (Figure 1b,c).

High-resolution transmission electron microscopy (HRTEM) analysis revealed no discernible lattice fringes within the nanosheets (NSs), indicating the absence of long-range crystallographic order and suggesting an amorphous structure. This was further confirmed by selected area electron diffraction (SAED, Figure 1d) and X-ray diffraction (XRD, Figure S1, Supporting

Information), both of which displayed broad, diffuse patterns lacking sharp diffraction peaks, characteristic of amorphous materials.

High-angle annular dark field scanning TEM (HAADF-STEM) micrographs and energy dispersive X-ray spectroscopy (EDS) compositional mapping confirmed a homogeneous distribution of Fe, Co, Ni, Mo, and W within the NSs (Figure 1e). The slight elemental segregation or enrichment at the NSs edges may arise from surface effects or imaging artifacts such as specimen tilt and thickness-induced variations in Z-contrast and EDS signal collection. Inductively coupled plasma optical emission spectroscopy (ICP-OES) analysis further revealed the elemental composition of the amorphous FeCoNiMoW HEANS to be Fe:Co:Ni:Mo:W = 10:8:37:17:28 (Figure S2, Supporting Information). Based on this specific metal ratio, the mixing entropy was calculated to be 1.5R, and the valence electron concentration (VEC) was determined to be 7.92.[8b]

By increasing the reaction time to 30 min, nanoparticles (NPs) began to nucleate and grow on the surface of the NSs (Figure S3, Supporting Information). After 120 min, the reaction yielded only NPs with sizes ranging from 20 to 70 nm (Figure 1f). This particle size increase resulted in a notably lower specific surface area for the crystalline HEANPs, measured at 43 $m^2\ g^{-1}$, compared to 114 $m^2\ g^{-1}$ for the amorphous HEANS (Figure S4, Supporting Information).

HRTEM imaging and fast Fourier transform (FFT) analysis revealed a well-defined atomic lattice, consistent with the face-centered cubic (FCC) FeCoNi phase (Figure 1g–i). This crystallinity was further confirmed by XRD, which showed clear diffraction peaks corresponding to an FCC structure (Figure S1, Supporting Information).

HAADF-STEM micrographs and EDS elemental maps confirmed a homogeneous distribution of Fe, Co, Ni, Mo, and W within the crystalline HEA nanoparticles (HEANP) (Figure 1j). In addition, ICP-OES analysis revealed the elemental composition of the HEANP to be Fe:Co:Ni:Mo:W = 18:16:21:22:23 (Figure S2, Supporting Information). Based on this composition, the mixing entropy was calculated to be 1.6 R, and the VEC was 7.68.

Taking into account the observed evolution in morphology, lattice structure, and composition, we hypothesize that the metal ions are rapidly and simultaneously reduced, leading to the formation of FeCoNiMoW HEAs with a kinetically driven NS architecture and random atomic distribution. The growth in the vertical (thickness) dimension of the NSs appears to be constrained by the adsorption of oleylamine (OAm) used as a solvent and the released CO,[16] as evidenced by Fourier transform infrared (FTIR) spectroscopy (Figure S5, Supporting Information). The presence of CO was found to be crucial for NS formation: in its absence, i.e., when $Mo(CO)_6$ and $W(CO)_6$ were not used as precursors, only ternary FeCoNi NPs, rather than NSs, were formed (Figure S6, Supporting Information). This highlights the key role of CO as a structure-directing agent in the synthesis of 2D nanomaterials, in agreement with previous reports.[17]

Overall, the 2D amorphous HEANSs were synthesized within a dynamically controlled reaction environment, in which the co-reduction of multiple metal precursors, CO release, and ligand coordination occur simultaneously to influence nucleation and growth. Specifically, the thermal decomposition of $Mo(CO)_6$ and $W(CO)_6$ not only provides Mo and W atoms but also releases CO in situ, which plays a key role in directing the 2D nanosheet morphology by selectively adsorbing on low-energy facets, limiting vertical growth, and stabilizing planar structures. Simultaneously, OAm serves both as a solvent and a coordinating ligand that further suppresses crystal growth in the thickness direction. The rapid and concurrent reduction of Fe, Co, Ni, Mo, and W ions favors the formation of a homogeneous HEA with random atomic distribution, while the fast nucleation kinetics and surface interactions suppress atomic rearrangement, thus yielding an amorphous structure. These synergistic effects enable the simultaneous realization of three key structural features, high-entropy composition, two-dimensional morphology, and amorphous nature, in the early stage of the reaction.

As the reaction time increases, Ostwald ripening becomes the dominant mechanism driving NP growth. During this process, the initially formed NSs gradually transform into NPs with lower surface energy, facilitated by atomic migration and rearrangement toward more thermodynamically stable configurations. This transformation is further promoted by the decrease in CO concentration, resulting from the continuous Ar flow, which diminishes the stabilization of specific crystallographic orientations on the NS surfaces. As a result, the combined effect of reduced surface stabilization and atomic rearrangement leads to the evolution from amorphous NSs to crystalline NPs over time. These NPs adopt the thermodynamically favorable FCC crystal structure, in agreement with the calculated VEC values.[8b]

### 2.2. Characterization of HEA-Modified Separators

HEAs were coated on one side of a polypropylene (PP) membrane to serve as functional separators in LSB cells. Scanning electron microscopy (SEM) images revealed that the HEANS/PP separator exhibits a rough surface morphology with an ≈20 µm-thick HEANS film (Figure S7, Supporting Information).

Contact angle measurements (**Figure 2a**) indicated that the HEANS/PP separator possesses significantly improved wettability toward the LSB electrolyte, with a contact angle of only 8.1°, compared to 86.1° for the pristine PP separator and 16.9° for the HEANP/PP separator. The enhanced wettability of HEANS is attributed to its higher surface energy, which is expected to facilitate Li-ion transport and reduce polarization during battery operation. Consistently, the HEANS/PP separator demonstrated a higher ionic conductivity of 0.05 S $m^{-1}$, outperforming both the pure PP separator (0.004 S $m^{-1}$) and the HEANP/PP separator (0.01 S $m^{-1}$) (Figure 2b).

The polysulfide adsorption capability of HEANS and HEANP was qualitatively assessed by dispersing equal amounts of each material in vials containing a 5 mM $Li_2S_4$ solution. Visual observation showed a more significant color fading in the HEANS-treated solution, indicating stronger polysulfide adsorption (Figure 2c). This was further confirmed by UV-vis spectroscopy of the supernatants, which showed that HEANS were more effective than HEANP in trapping LiPS (Figure 2d). The ability of HEANS to block polysulfide migration was further validated using an H-type diffusion cell with a $Li_2S_4$ concentration gradient. When PP or HEANP/PP separators were used, the initially colorless solution in the receiving half-cell gradually turned yellow over time, indicating LiPS diffusion. In

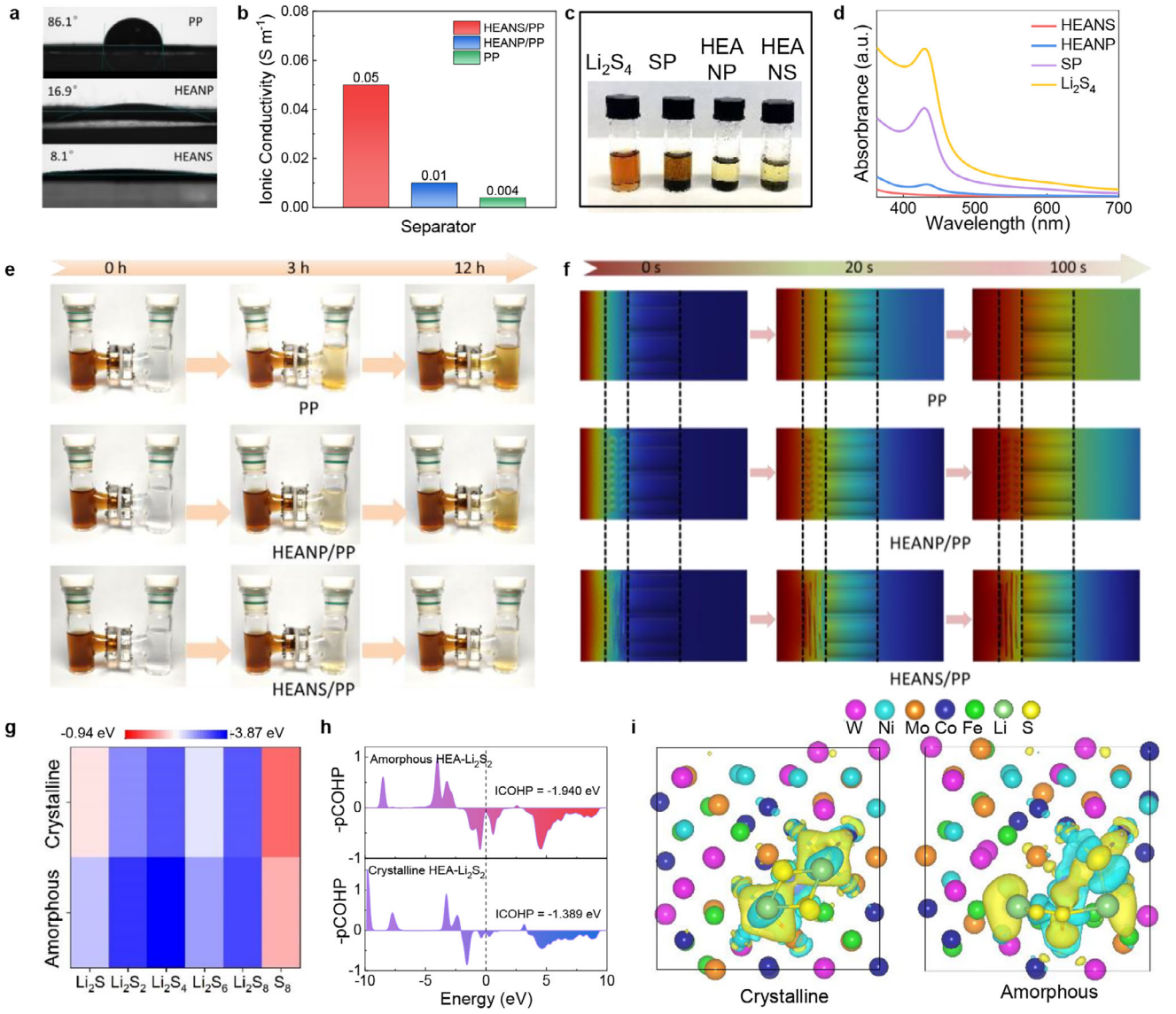


**Figure 2.** Characterization of HEA-modified separators. a) Contact angle and b) ion conductivity of PP, HEANP/PP, and HEANS/PP separators in electrolyte of 1.0 M LiTFSI in 1,3-dioxolane (DOL) and 1,2-dimethoxyethane (DME) (V/V = 1:1) with 2 wt.% $LiNO_3$ additive. c) Optical images and d) UV-vis spectra of polysulfide ($Li_2S_4$) solution containing 10 mg of the different adsorbers after 12 h of polysulfide adsorption. e) Photographs of H-type glass cells with PP, HEANP/PP, and HEANS/PP separators after different diffusion times. Initially, only the left cell contained $Li_2S_4$ at a 10 mM concentration. f) Results of the finite element simulations of the polysulfide diffusion process in different separators. g) Adsorption energies of various sulfur species on the surface of HEANS and HEANP. h) iCOHP analysis of $Li_2S_2$ adsorbed on the surface of HEANS and HEANP. i) CDD images in HEANS and HEANP with an adsorbed $Li_2S_2$. The contour around the atoms represents electron accumulation (yellow) or electron depletion (blue).

contrast, the HEANS@PP separator effectively inhibited polysulfide transport, with no noticeable color change observed after 12 h (Figure 2e).

While minor, the particle geometry and distribution can also have an effect on the diffusion and release of the polysuflides to the electrolyte. To show this, COMSOL finite element simulation based on physical diffusion model were used to evaluate the LiPS migration on different structures for separators, in which the transport of diluted species in a porous media interface module (same model width and diffusion depth, details shown in SI 1.4 part) was adopted to simulate the diffusion process of polysulfides across different layer structures (PP layer, HEANS/PP, and HEANP/PP, with the same material amount loading). Consistent with the experimental results, the simulation results showed that the HEANS/PP separator exhibited superior blocking effects on polysulfide diffusion compared with the pure PP layer and HEANS/PP configurations (Figure 2f).

The influence of crystal structure and atomic organization in FeCoNiMoW HEA materials on LiPS adsorption was investigated using DFT calculations. Optimized structural models of both the amorphous and crystalline HEAs are presented in Figures S8 and S9 (Supporting Information). Both the amorphous and crystalline HEAs exhibit strong binding interactions with various sulfur-containing species. Notably, the amorphous HEA

demonstrates higher adsorption energies for all evaluated S and Li–S species, from $S_8$ to $Li_2S$ (Figure 2g).

DFT calculations further reveal that the d-band center positions of the amorphous and crystalline FeCoNiMoW HEAs are located at 1.365 and 1.782 eV, respectively (Figure S10, Supporting Information). These values indicate that both materials act as electron acceptors, capable of binding LiPSs, which exhibit electron-donating character. Importantly, the d-band center of the amorphous HEA lies closer to the Fermi level than that of the crystalline counterpart. This proximity enhances the interaction with LiPSs, facilitating stronger adsorption and more effective polysulfide trapping.

Taking $Li_2S_2$ adsorption as a representative case, the integrated crystal orbital Hamilton population (iCOHP) analysis reveals the stronger bonding interaction and the tighter chemical bond between the amorphous HEANS and $Li_2S_2$ compared with that of the crystalline HEANP (Figure 2h). In addition, differential charge density (CDD) maps show more pronounced charge transfer between $Li_2S_2$ and the amorphous HEA, compared to the crystalline counterpart (Figure 2i).

Overall, these theoretical results align with experimental findings, confirming that FeCoNiMoW HEANS exhibits superior LiPS adsorption capability relative to HEANP. The amorphous structure of HEANS modulates the electronic states near the Fermi level, enhancing interaction with LiPS and contributing to suppress the shuttle effect in Li–S batteries.

The S 2p X-ray photoelectron spectroscopy (XPS) spectrum of amorphous HEANS after $Li_2S_4$ adsorption revealed four distinct doublets (Figure S11a, Supporting Information). In the lower binding energy region (161–165 eV), two pairs of S 2p peaks were attributed to terminal ($S_T$) and bridging ($S_B$) sulfur species in the adsorbed LiPSs. In the higher binding energy region (166–171 eV), the two additional doublets were assigned to thiosulfate and polythionate species. Following $Li_2S_4$ adsorption, the XPS spectra of all metallic elements in the HEANS exhibited slight shifts toward lower binding energies (Figures S11b–f, S12, Supporting Information), indicating electron transfer from LiPS to the metal sites. This shift supports the formation of chemical bonds between the HEA metal atoms and S atoms from $Li_2S_4$. Notably, the W 4f core level displayed a significantly larger binding energy shift, suggesting a stronger interaction between W and S, which may be attributed to the higher electronegativity of W compared to the other metal constituents.

### 2.3. Catalyzed Li–S Reaction Analysis

To evaluate the electrocatalytic activity of the synthesized HEAs, they were used as electrode materials in symmetric cells containing a $Li_2S_6$-based electrolyte (see SI for experimental details). For this analysis, electrodes were prepared by loading FeCoNiMoW HEANS and HEANP catalysts onto carbon paper (CP), resulting in HEANS@CP and HEANP@CP electrodes. A carbon-based Super P (SP) electrode was also tested as a reference (SP@CP). In control experiments conducted without $Li_2S_6$, the symmetric cells exhibited negligible current response, confirming that the observed currents in $Li_2S_6$-containing systems arise exclusively from electrocatalytic redox reactions of lithium polysulfides (LiPSs), rather than from capacitive contributions.

Cyclic voltammetry (CV) measurements of the $Li_2S_6$-containing symmetric cells (**Figure 3a**) displayed the characteristic LiPSs redox peaks. Two distinct pairs of redox peaks can be observed at −0.24/0.24 and −0.43/0.43 V for the HEPNS-based cell, attributed to the multisteps for LiPSs conversion process. In comparison, the CV curve of the HEANP-based cell exhibits the two broader redox peaks at −0.1/0.1 and −0.68/0.68 V, while the cell based on SP suffers from even more severe polarization and exhibits no clear redox peaks. Among all tested electrodes, the HEANS-based cell exhibited the highest current density and largest integrated area, indicating superior electrocatalytic activity and a more efficient LiPS conversion process compared to both HEANP and SP electrodes.

The potentiostatic intermittent titration technique (PITT) was employed to evaluate the reaction kinetics of the $Li_2S_4 \rightarrow Li_2S$ conversion, a critical step that significantly impacts the overall capacity performance of LSBs (see SI for experimental details). For this analysis, HEA-based electrodes were paired with lithium foil anodes within coin-type cells. The discharge process was then monitored to assess the kinetics of $Li_2S$ formation on the different catalytic surfaces.

As shown in Figure 3b, when applying a constant voltage of 2.09 V, the HEANS@CP electrode exhibited a higher current response than the HEANP@CP electrode, although no nucleation peak was observed for either, indicating that nucleation of $Li_2S$ had not yet commenced. Upon decreasing the voltage to 2.06 V, nucleation peaks appeared for both electrodes, with the HEANS@CP electrode showing an earlier onset and a higher current density, suggesting a faster $Li_2S$ nucleation and growth process compared to HEANP. At a further reduced voltage of 2.03 V, the HEANP@CP electrode displayed a more pronounced nucleation peak, indicating that significant $Li_2S$ formation was still ongoing. This suggests that lower potentials or longer durations are required for complete $Li_2S$ nucleation on the crystalline HEANP surface, whereas the amorphous HEANS facilitates faster and more complete conversion at lower overpotentials. Integrating the whole current, from 2.09 to 2.03 V, the HEANS@CP electrode delivered a higher specific capacity of 1055.8 mAh $g^{-1}$, compared to 882.9 mAh $g^{-1}$ for the HEANP@CP electrode, highlighting a more efficient liquid-to-solid conversion during LiPS reduction.

Coin-type LSBs were assembled using an S@SP cathode electrode (sulfur loading:1.0 mg $cm^{-2}$, preparation process can be found in SI and Figure S13, Supporting Information), a lithium foil anode, and one of three separators: uncoated PP, or PP membranes coated with either HEANS or HEANP (see SI for experimental details). The CV curves obtained at a scan rate of 0.1 mV $s^{-1}$ over the initial three cycles are shown in Figures S14–S16 (Supporting Information). Following the first cycle, both HEA-modified separators (HEANS/PP and HEANP/PP) enabled a highly reproducible CV response in subsequent cycles, reflecting superior electrochemical reversibility and effective promotion of the Li–S conversion reactions. In contrast, the cell with the unmodified PP separator showed a marked decline in performance over cycling, attributed to the absence of LiPS adsorption and lack of catalytic activation.

A direct comparison of the third-cycle CV curves for all three cells is presented in Figure 3c. Among them, the cell with the HEANS/PP separator exhibited cathodic peaks with the highest

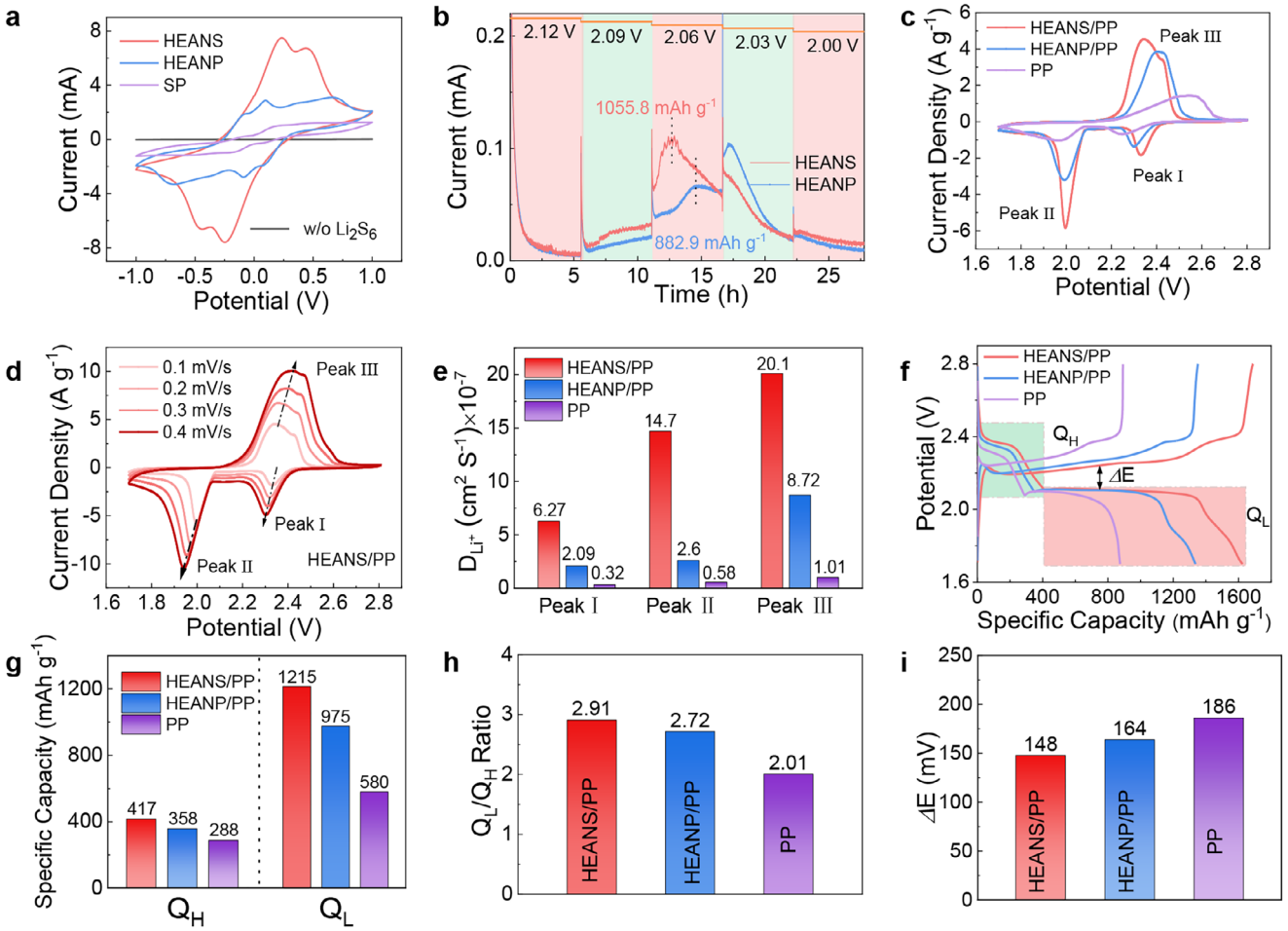


**Figure 3.** Catalyzed Li–S reaction performance. a) CV curves of symmetrical cells based on HEANS@CP, HEANP@CP, and SP@CP electrodes. b) PITT curves. c) CV curves of LSBs with HEANS/PP, HEANP/PP, and uncoated PP separators. d) CV curves of LSB cells with a HEANS/PP separator at different scan rates. e) $D_{Li^+}$ of LSB cells with HEANS/PP, HEANP/PP, and uncoated PP separator calculated from peaks I, II, and III. f) GCD profiles at 0.1C, g) $Q_H$ and $Q_L$, h) $Q_L/Q_H$ ratios, and i) ΔE values of LSBs with HEANS/PP, HEANP/PP, and uncoated PP separator.

current densities and located at the lowest potentials, indicating enhanced LiPS reduction kinetics and more efficient sulfur conversion.

CV curves at different scan rates were used to analyze the LiPS redox reaction kinetics (Figure 3d, Figures S17,S18, Supporting Information). As shown in Figures S19–S21 (Supporting Information), all LSBs exhibited $Li^+$ diffusion-limited reactions with the peak currents ($I_p$) showing a linear dependence with the square root of the scan rate ($v$).[1a,18] Thus the classical Randles-Sevcik equation was used to calculate the $Li^+$ diffusivity.[19]

$$I_p = \left(2.6910^5\right) n^{1.5} A D_{Li^+}^{0.5} C_{Li^+} v^{0.5} \quad (1)$$

where n is the charge transfer number, A is the geometric electrode area, $D_{Li^+}$ is the $Li^+$ diffusion coefficient, and $C_{Li^+}$ is the concentration of $Li^+$ in the electrolyte.

The cells with a HEANS/PP separator exhibited the highest $D_{Li^+}$ values at $6.27 \times 10^{-7}$, $1.47 \times 10^{-6}$, and $2.01 \times 10^{-6}$ $cm^2\ S^{-1}$ for peaks I, II, and III, respectively, which were between 2 and 25 times higher than those of cells equipped with HEANP/PP and uncoated PP separators, respectively (Figure 3e). The $Li^+$ diffusivity is in part related to the viscosity of the electrolyte containing dissolved LiPS and the accumulation of insulating $Li_2S_2/Li_2S/S_8$. Therefore, the higher $D_{Li^+}$ of cells based on HEANS/PP separators reflects a lower LiPS concentration in the electrolyte and a thinner or more homogeneous layer of solid active materials, which denotes an improved LiPS reaction kinetics.

The galvanostatic charge/discharge (GCD) profiles of the assembled cells at 0.1C are shown in Figure 3f. All cells display the characteristic two discharge plateaus and one charge plateau, consistent with the redox peaks observed in the CV curves (Figure 3c). Among the tested systems, the HEANS/PP-based cell delivered the highest specific capacity, reaching 1632 mAh $g^{-1}$, significantly outperforming the HEANP/PP cell (1333 mAh $g^{-1}$) and the cell with an uncoated PP separator (868 mAh $g^{-1}$).

During discharge, $Q_H$ and $Q_L$ represent the capacities associated with the high-voltage plateau and low-voltage plateau, respectively. $Q_H$ corresponds to the reduction of sulfur to soluble $Li_2S_4$ ($S_8 + 4Li^+ + 4e^- \rightarrow 2Li_2S_4$), while $Q_L$ reflects the further reduction of $Li_2S_4$ to insoluble $Li_2S$ ($2Li_2S_4 + 12Li^+ + 12e^- \rightarrow 8Li_2S$). As shown in Figure 3g, both $Q_H$ and $Q_L$ values were

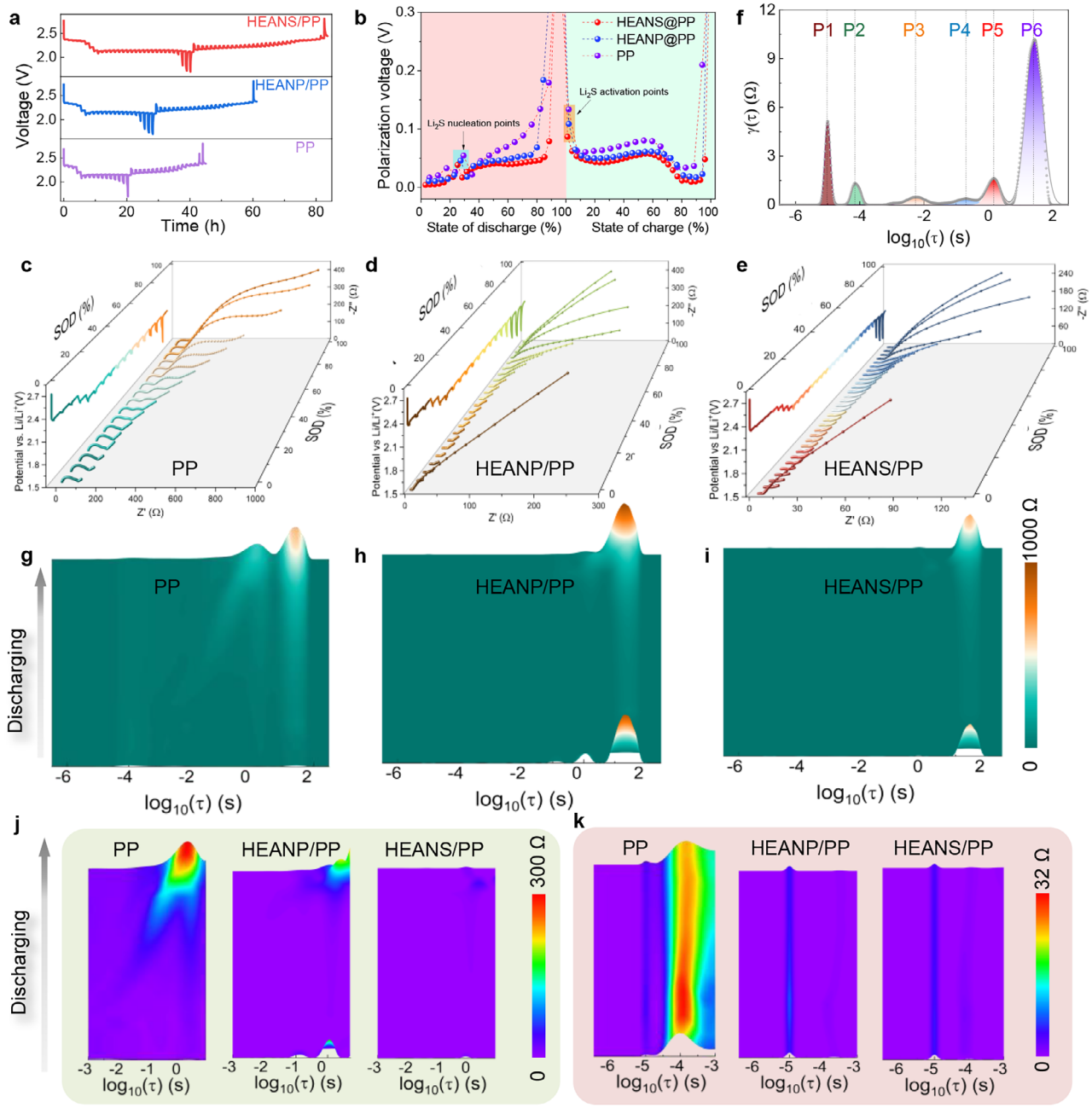


**Figure 4.** In situ GITT-EIS analysis of LSBs with uncoated PP, HEANP/PP, and HEANS/PP separators. a) GITT curves. b) Polarization voltages. c–e) In situ EIS spectra. f) Representative DRT spectrum from HEANS/PP sample at 3.3% DOD. g–i) DRT spectra at different DOD. j–k) Enlarged DRT spectra at different DOD.

highest in the HEANS/PP-based cell, indicating a more complete and efficient conversion of $S_8$ to long-chain polysulfides, and ultimately to $Li_2S$. Additionally, the $Q_L/Q_H$ ratio was 2.91 for the HEANS/PP cell, approaching the theoretical maximum of 3 (Figure 3h). This implies that a high proportion of sulfur underwent full reduction with minimal polysulfide loss, highlighting the superior catalytic activity of HEANS in promoting deep sulfur conversion.

The voltage gap (ΔE) between the charge plateau and the second discharge plateau at 50% state of discharge was used to assess voltage polarization. The HEANS/PP-based LSB exhibited the lowest ΔE value of 148 mV (Figure 3i), indicating reduced polarization and more favorable LiPS conversion kinetics, further reinforcing the performance advantage of the HEANS-modified separator.

In situ GITT-EIS measurements were conducted after three activation cycles at 0.1C, by applying a 20-minute galvanostatic discharge pulse followed by a one-hour relaxation period (**Figure 4a**). EIS spectra were recorded during the relaxation period (Figure S22, Supporting Information). As commonly

observed, the polarization voltage, defined as the difference between the voltage at the end of relaxation and the voltage at the end of the discharge pulse, reached a maximum at the end of the first discharge plateau and progressively increased with the depth of discharge (DOD), exhibiting a sharp rise at the end of the second discharge plateau (Figure 4b). During charging, after an initially high polarization, the polarization voltage stabilized and decreased during the final charging plateau, corresponding to the conversion of LiPS back to $S_8$. Notably, LSBs employing HEANS/PP separators exhibited significantly lower polarization voltages throughout the entire GCD profile, indicating improved conversion kinetics and reduced internal resistance.

Figure 4c–e display the Nyquist plots of the in situ EIS spectra for the various cells during discharge, recorded during the GITT measurements. The EIS spectrum at 0% DOD corresponds to the cell fully charged to 2.8 V. Three characteristic features can be observed: i) a high-frequency semicircle attributed to the internal resistance of the cell; ii) a second semicircle in the mid-frequency region, associated with the charge transfer resistance at the cathode-electrolyte interface related to the Li–S reaction; and iii) a sloped line in the low-frequency region, corresponding to $Li^+$ diffusion. The first semicircle remained nearly unchanged throughout the discharge process, while the second semicircle increased in size, and the slope of the low-frequency region gradually decreased with increasing DOD (Figures S23 and S24, Supporting Information). Notably, cells utilizing HEANP/PP (Figure 4d) and, especially, HEANS/PP (Figure 4e) separators exhibited significantly lower internal and charge transfer resistances, along with enhanced $Li^+$ diffusion kinetics. These results support the role of HEAs in accelerating Li–S conversion reactions.

DRT analysis was employed to deconvolute the overlapping relaxation processes contributing to the EIS spectra and to better resolve the distinct electrochemical mechanisms involved (see SI, Figure 4f; Figure S25, Supporting Information).[20] For each process, a characteristic time constant ($\tau$) was determined, along with the area under each peak, which reflects the specific polarization resistance (Table S2, Supporting Information).[21]

The P6 peak ($\tau$ = 26 s, $\log_{10}\ \tau$ = 1.42) corresponds to $Li^+$ diffusion in solid sulfur species ($S_8/Li_2S_2/Li_2S$).[20b,22] At 0% DOD, a strong P6 peak in HEANS/PP and HEANP/PP cells indicates efficient LiPS-to-$S_8$ conversion during charging, unlike the PP-based cell, which showed limited $S_8$ presence (Figure 4g–I; Figure S26, Supporting Information). During mid-discharge (15–80% DOD), higher P6 intensity in HEANP/PP and PP cells suggests greater diffusion resistance due to less favorable $Li_2S_2/Li_2S$ deposition. In contrast, HEANS/PP promotes more uniform nucleation, enabling faster $Li^+$ diffusion. At full discharge (100% DOD), all cells exhibited increased P6 intensity due to insulating $Li_2S_2/Li_2S$ formation, but the HEANS/PP cell still showed the lowest diffusion resistance, attributed to its higher catalytic activity and larger active surface area.

The peaks P3-P5 ($\tau$ = 6 ms to 1 s; $\log_{1n}\ \tau$ = −2.2 to 0.1) are associated with the charge transfer resistance of the Li–S redox reaction at the cathode.[20c,23] As the DOD increased, their intensities also increased, indicating progressively hindered discharge kinetics (Figure 4j). Notably, the HEANS/PP-based LSB consistently exhibited the lowest charge transfer resistance throughout the discharge, attributed to the abundant and highly active catalytic sites in HEANS that promote Li–S conversion. Additionally, distinct P3–P5 peaks were observed at 0% DOD in the HEA-based cells, but not in the PP-based cell, indicating a more complete prior conversion to $S_8$, and thus a slower initial reduction reaction.

P2 ($\tau$ = 80 µs, $\log_{1n}\ \tau$ = −4.1) corresponds to the anode-electrolyte interphase resistance. The PP-based LSB exhibited a significantly higher P2 intensity compared to the HEANS/PP and HEANP/PP cells, attributed to greater LiPS crossover and subsequent lithium foil corrosion during activation (Figure 4k).[21b] This highlights the effectiveness of the HEA-modified separator layers in mitigating LiPS migration and anode degradation. Additionally, the P2 peak in the PP-based cell broadened with increasing DOD, indicating an increasingly unstable interfacial charge transfer process.

Finally, P1 ($\tau$ = 10 µs, $\log_{1n}\ \tau$ = −5.0) was attributed to the electrode inter-particle resistance, influenced by the carbon/sulfur composite and binder components.[20a,24] This peak remained similar across all three LSBs and showed negligible change during the discharge process (Figure 4k).

In situ Raman spectroscopy was used to investigate the LiPS diffusion at the anode side of the separator during the discharge process (Figures S27,S28a, Supporting Information). In the LSB equipped with the uncoated PP, at 2.3 V, the $S_8^{2-}/S_6^{2-}$ signals at 221.6/400.9 $cm^{-1}$ were observed. Throughout the discharge process, $S_2^{2-}/S_4^{2-}$ signals at 453.1 $cm^{-1}$ gradually emerged, accompanied by a weakening of the $S_8^{2-}$ signal.[25] The $S_6^{2-}$ signal almost maintained consistent intensity during the discharge process, even as discharge approached termination (1.9 V). This implies that once a portion of $S_6^{2-}$ diffuses to the anode, it encounters substantial difficulty returning to the cathode to re-engage in subsequent redox reactions. Notably, in the HEANS/PP-based cells, no detectable signal of sulfur-containing species was observed at the anode side, indicating effective suppression of LiPS migration across the separator (Figure S28b, Supporting Information).

### 2.4. LSB Performance

The GCD profiles of LSBs at various current densities, from 0.1C to 10C, are displayed in **Figure 5**a and Figures S29,S30 (Supporting Information). HEANS/PP-based LSBs showed outstanding rate performance with two clear discharge plateaus at all current rates up to 10C and significantly higher capacities than the reference cells at all rates, with 614 mAh $g^{-1}$ maintained at 10C (Figure 5b). When switched back to 0.2C, the capacity recovered to 1479 mAh $g^{-1}$, corresponding to 99.5% capacity retention. In contrast, the PP-based LSBs underwent rapid capacity fading, with no capacity recorded at a current rate of 5C.

The energy conversion efficiency ($\eta$) was determined from the ratio of the total energy output during discharge to the energy input during charge, calculated by integrating the product of potential (U) and current (I) over time for both processes:[26]

$$\eta = \frac{E_{out}}{E_{in}} = \frac{\int UIdt}{\int UIdt} \quad (2)$$

In the 0.1C–0.5C range, HEA-based LSBs exhibited energy conversion efficiencies exceeding 90%, which gradually declined

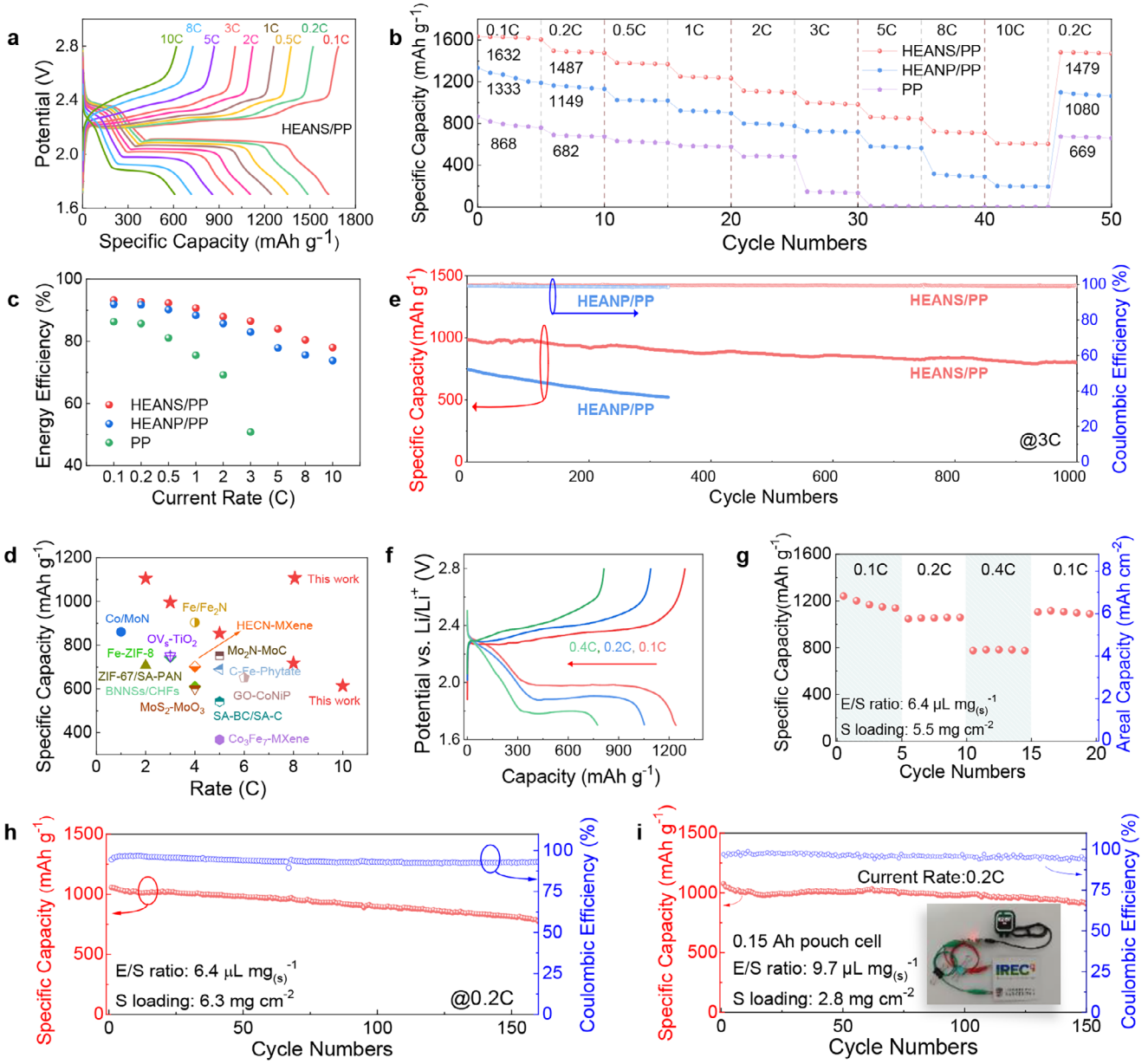


**Figure 5.** LSB performance. a) GCDs curves at different rates. b) Specific capacity at different current rates. c) Round trip energy efficiencies. d) Comparison of specific capacity versus current rate for recently reported LSBs, highlighting the superior rate performance of the HEANS/PP-based cell. e) Long-term cycling performance at 3C. f) GCDs curves at different rates of a HEANS/PP-based LSB with a sulfur loading of 5.5 mg $cm^{-2}$. g) Specific capacity and areal capacity at different current rates. h) Long-term cycling performance at 0.2C of a HEANS/PP-based LSB with a sulfur loading of 6.3 mg $cm^{-2}$. i) Cycling performance of a HEANS/PP-based pouch cell. The inset shows a digital photo of the pouch cell charging a smartwatch.

with increasing C-rate due to rising overpotentials of the Li–S reaction, reaching ≈80% at 10C in the HEANS/PP cell (Figure 5c). In contrast, the PP-based cell showed significantly lower efficiencies, starting around 85% at 0.1C and dropping sharply to 50% at 3C. The superiority of the HEANS interlayer is demonstrated by comprehensive comparison with recently reported LSB functionalized separators and electrocatalysts (Figure 5d; Figures S31,S32 and Tables S3,S4, Supporting Information). Specifically, HEANS achieves the highest capacity across all C-rates tested, showcasing excellent catalytic activity and strong polysulfide conversion capability even under high-rate conditions up to 10C. This outstanding rate capability can be attributed to the amorphous nature and 2D nanosheet structure, which facilitate fast electron/ion transport and strong chemical confinement of soluble LiPS.

Figure 5e presents the long-term GCD cycling performance of HEA-based LSBs at 3C. The HEANS/PP-based cell exhibited excellent stability, with a high initial capacity of 998 and 814 mAh $g^{-1}$ retained after 1000 cycles, corresponding to an average capacity loss of only 0.018% per cycle. Additionally, the coulombic efficiency remained above 99.8% throughout the test. The

HEANP/PP-based cell showed an initial capacity of 742 mAh $g^{-1}$, retaining 515 mAh $g^{-1}$ after 330 cycles, with an average capacity loss of 0.1% per cycle and a decrease in coulombic efficiency from 99.3% to 98.5%. Enhanced performance was also observed for the HEANS/PP-based LSB at a higher current rate of 5C (Figure S33, Supporting Information). In contrast, the LSB using an unmodified PP separator delivered an initial capacity of 568.8 mAh $g^{-1}$, with a higher average capacity fading rate of 0.16% per cycle over 200 cycles at 1C (Figure S34, Supporting Information).

For practical applications, Li–S batteries require high sulfur loadings (>5 mg $cm^{-2}$) and reduced electrolyte volumes (<10 µL mg $_S^{-1}$). To assess performance under these conditions, electrochemical tests were conducted on HEANS/PP-based LSBs with sulfur loadings of 5.5 and 6.3 mg $cm^{-2}$ and an electrolyte-to-sulfur (E/S) ratio of 6.4 µL $mg_S^{-1}$. Figure 5f,g shows the rate performance of the cell with 5.5 mg $cm^{-2}$ sulfur loading. The GCD profiles from 0.1C to 0.4C exhibit one charge and two discharge plateaus, indicating efficient LiPS redox reactions and moderate polarization. A high initial discharge capacity of 1241 mAh $g^{-1}$ (6.83 mAh $cm^{-2}$) was achieved at 0.1C, approximately 1.7 times the areal capacity of commercial Li-ion batteries (≈4 mAh $cm^{-2}$). At 0.4C, a stable capacity of 782 mAh $g^{-1}$ was maintained, and upon returning to 0.1C, 90% of the initial capacity (1115 mAh $g^{-1}$) was recovered.

For cells with an even higher sulfur loading of 6.3 mg $cm^{-2}$ (Figure 5 h; Figure S35, Supporting Information), a capacity of 775 mAh $g^{-1}$ (4.9 mAh $cm^{-2}$) was retained after 160 cycles at 0.2C, ≈75% of the initial value, corresponding to a low average capacity fade of 0.15% per cycle. These results confirm that HEANS/PP-based LSBs can operate stably under high-loading and lean-electrolyte conditions.

To further demonstrate the practical applicability of the HEANS/PP separator, pouch cells were assembled and tested. As shown in Figure 5i, the pouch cell successfully powered a smartwatch via a voltage upconversion step, confirming its real-world utility. The electrochemical performance of the HEANS/PP-based pouch cell, cycled at 0.2C, is also presented in Figure 5i. The cell delivered an initial capacity of 1075.8 mAh $g^{-1}$ and retained 85.4% of its capacity after 150 cycles (Figure S36, Supporting Information), highlighting its excellent cycling stability and practical viability.

### 2.5. Thermodynamic Calculations

DFT calculations were used to thermodynamically analyze the catalytic process for both crystalline and amorphous HEA and determine the influence of the crystal structure and corresponding electron structure on the LSB performance. To determine the most efficient active sites in the HEANS, the activity of the different metals to activate the LiPS redox reaction was experimentally tested using the different commercial metal nanopowders (Fe, Co, Ni, Mo, and W), all having similar average particle sizes. As shown in Figure S37 (Supporting Information), the symmetrical cells based on W electrodes showed the highest current density, implying the most efficient LiPS conversion process. This result is consistent with XPS spectra showing W to undergo the largest binding energy shift upon LiPS adsorption on the HEA. A comparative experiment with FeCoNiMo showed a notable drop in discharge capacity (Figure S38, Supporting Information), highlighting W playing an essential role in LiPS conversion. Thus, W was selected as the preferential site to carry out additional DFT calculations.

The step-by-step free energy diagram of the $S_8$ transformation to $Li_2S$ for both amorphous and crystalline HEA is shown in **Figure 6a**. The transformation from $Li_2S_4$ to $Li_2S_2$ is calculated to be the rate-determining step (RDS) for both amorphous and crystalline HEA, which is consistent with previous works showing $Li_2S_4$ to be a key electrochemical intermediate controlling the overall sulfur reduction reaction kinetics and overpotential, particularly in the more sluggish second reduction stage ($Li_2S_4 \rightarrow Li_2S_2 \rightarrow Li_2S$).[27] The energy barrier of the RDS for amorphous HEA (1.48 eV) is significantly lower than that of crystalline HEA (1.71 eV), indicating a more efficient LiPS conversion process and faster reaction kinetics on the former.

Each step in the complex polysulfide conversion reactions involves the cleavage of S–S bonds and the formation of new Li–S bonds. These sub-reactions are already inherently intricate and may proceed through intermediate transition states that dominate the reaction pathway. Therefore, the energies of the initial and final polysulfide species alone are not always reliable indicators of reaction favorability, as is often assumed. To illustrate this, we show that $Li_2S_4$ does not convert directly to $Li_2S_2$, but instead passes through a defined transition state (TS, Figure 6b) en route to a more thermodynamically stable configuration. The detailed conversion step for the amorphous and crystalline HEA, and the enthalpic decomposition energy barrier are shown in Figure 6c,d. The enthalpy change for the $Li_2S_4$ adsorbed on the amorphous HEA to evolve to the TS is 0.63 eV, while it is significantly larger, up to 0.96 eV, on the surface of the crystalline HEA. The iCOHP of Li–S bond for $Li_2S_4$ adsorbed on both amorphous and crystalline HEA were further calculated to be 0.077 eV and 0.101 eV respectively, proving a relatively weak Li–S bond strength for $Li_2S_4$ adsorbed on amorphous HEA, i.e., an easier transformation to $Li_2S_2$ (Figure 6e). Overall, amorphous HEA shows a lower RDS energy barrier by decreasing the decomposition energy barrier, thus accelerating the LiPS thermodynamic conversion process.

Compared with FeCoNiMoW HEANS-based LSBs, the medium-entropy counterparts (FeCoNi and FeCoNiMo) exhibit significantly inferior electrochemical performance (Figure S38, Supporting Information). This comparison underscores the beneficial role of the combination of multiple metals in enhancing catalytic activity with a broader distribution of active sites. Besides, FeCoNiMoW HEANS possess an amorphous structure and 2D nanosheet morphology, which together provide a higher density of unsaturated active sites, improved $Li^+$ transport, and enhanced surface accessibility. These structural features result in favorable electronic states (e.g., closer d-band position to the Fermi level), and a lower energy barrier for the rate-determining $Li_2S_4 \rightarrow Li_2S_2$ step. Therefore, the high performance is attributed to composition (5d element for W), crystallographic (amorphous), and architectural parameters (2D), which is distinct from previously reported HEA systems with main 3d elements.[12,28] In particular, 5d metal W plays a significant role as a strong Lewis acidic site, significantly enhancing the chemical adsorption and activation of LiPS. This finding reveals a previously underexplored but highly effective catalytic

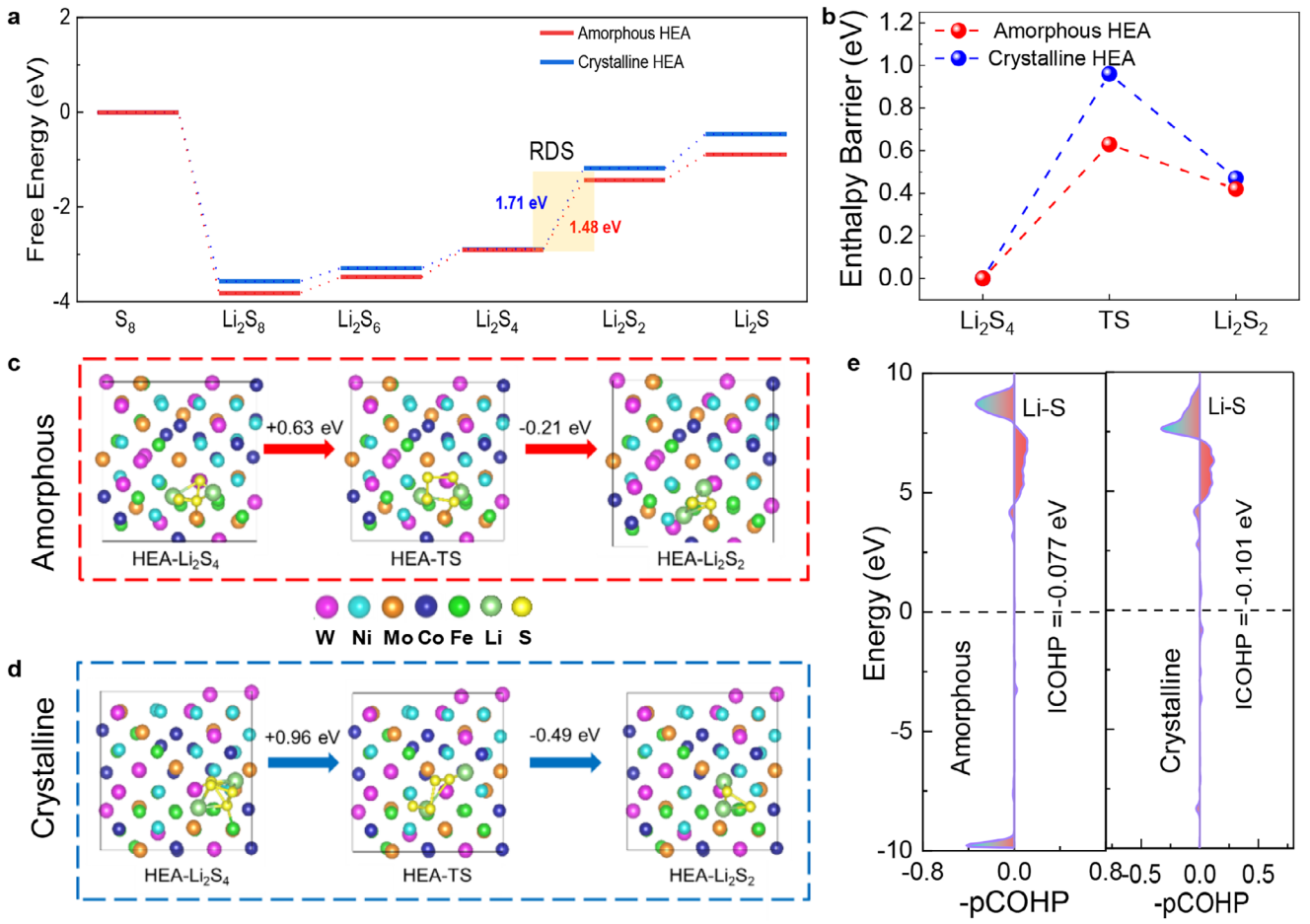


**Figure 6.** DFT calculations. a) Free energy evolution and related energy barrier in the conversion from $S_8$ to $Li_2S$. b) Enthalpy barrier of $Li_2S_4$ absorbed on amorphous and crystalline HEA transferred to TS and then converted to $Li_2S_2$. c,d) Corresponding models of the $Li_2S_4$ absorbed on the amorphous and crystalline HEA transferred to TS and then converted to $Li_2S_2$ from the top view. e) iCOHP analysis of Li–S bond of $Li_2S_4$ adsorbed on the surface of the amorphous and crystalline HEA.

process, showing that W-centered active sites, when embedded in an amorphous high-entropy environment, can outperform conventional transition-metal-based HEAs in promoting LiPS conversion.

## 3. Conclusion

Amorphous HEANS and crystallized HEANP FeCoNiMoW were controllably synthesized through a colloidal method with a surface confinement strategy to tailor their dimensions, sizes, crystallinity, and electronic structures. Amorphous HEANS-modified separators exhibit significantly improved performance over their crystalline counterparts. The amorphous structural feature and two-dimensional morphology of HEANS provide a high specific surface area and abundant unsaturated active sites. They also modulate the electronic states near the Fermi level, thereby enhancing $Li^+$ diffusion, reducing charge transfer resistance, and promoting stronger LiPS adsorption. As a result, HEANS effectively reduces the LiPS migration and mitigates the shuttle effect. In situ analyses, including Raman spectroscopy, GITT-EIS, and DRT showed an accelerated reaction kinetics and a complete conversion from $S_8$ to $Li_2S$, thus optimizing the sulfur utilization and capacity release in HEANS. DFT calculations further unveiled that the amorphous HEANS catalyst lowers the decomposition energy barrier of the TS in the LiPS conversion process. Overall, compared with the crystallized HEANP phase, amorphous HEANS promotes a better LSB performance. This work offers a solid framework for understanding the catalytic mechanisms of HEAs in LiPS conversion, offering valuable insights into the structural influence of HEAs in LSB applications.

## Supporting Information

Supporting Information is available from the Wiley Online Library or from the author.

## Acknowledgements

The authors acknowledge support from the 2BoSS project of the ERA-MIN3 program with the Spanish grant number PCI2022-132985/AEI/10.13039/501100011033, and funding from Generalitat de

Catalunya 2021SGR01581 and European Union NextGenerationEU/PRTR. L.Yang, C.Huang, X.Lu, A.Yu, C.Li, J.Yu, and X.Bi thank the China Scholarship Council (CSC) for the scholarship support. This research was supported by the Scientific Service Units (SSU) of ISTA through resources provided by the Electron Microscopy Facility (EMF), and by the Werner Siemens Foundation (WSS) for financial support.

## Conflict of Interest

The authors declare no conflict of interest.

## Author Contributions

R.H., L.Y., C.Z., Y.Z., and A.C. performed conceptualization; R.H., L.Y., and C.Z. performed methodology; R.H. and L.Y. performed investigation; R.H., L.Y., S.L., Y.D., C.H., X.L., L.Z., A.Y., C.Z., C.L., X.B., Y.L., Y.l., J.L., A.O.M., S.Y., Y.X., M.I. performed visualization; Y.Z. performed software; C.Z., Y.Z., and A.C. performed supervision; R.H. wrote the original draft; L.Y., C.Z., and A.C. wrote, reviewed, and edited the draft.

## Data Availability Statement

The data that support the findings of this study are available from the corresponding authors upon reasonable request.

## Keywords

amorphous, high entropy alloy, in situ electrochemical impedance spectroscopy, in situ Raman, Li–S batteries

Received: June 1, 2025
Revised: July 23, 2025
Published online: August 6, 2025

[1] a) C. Zhang, J. J. Biendicho, T. Zhang, R. Du, J. Li, X. Yang, J. Arbiol, Y. Zhou, J. R. Morante, A. Cabot, *Adv. Funct. Mater.* **2019**, *29*, 1903824; b) W. Guo, W. Zhang, Y. Si, D. Wang, Y. Fu, A. Manthiram, *Nat. Commun.* **2021**, *12*, 3031.

[2] a) Y. Yang, B. Sun, Z. Sun, J. Xue, J. He, Z. Wang, K. Sun, Z. Sun, H. K. Liu, S. X. Dou, *Coordin. Chem. Rev.* **2024**, *510*, 215836; b) R. Guo, Y. Yang, X. L. Huang, C. Zhao, B. Hu, F. Huo, H. K. Liu, B. Sun, Z. Sun, S. X. Dou, *Adv. Funct. Mater.* **2023**, *34*, 2307108; c) C. Zhao, F. Huo, Y. Yang, J. Ruan, F. Chai, H. Xu, Y. Liu, L. Zhang, A. Cabot, Z. Sun, Y. Zhang, *Adv. Funct. Mater.* **2024**, 202402175.

[3] J. Yu, I. Pinto-Huguet, C. Y. Zhang, Y. Zhou, Y. Xu, A. Vizintin, J. J. Velasco-Velez, X. Qi, X. Pan, G. Oney, A. Olgo, K. Marker, M. D. S. L, Y. Luo, Y. Lu, C. Huang, E. Hark, J. Fleming, P. Chenevier, A. Cabot, Y. Bai, M. Botifoll, A. P. Black, Q. An, T. Amietszajew, J. Arbiol, *ACS Energy Lett.* **2024**, *9*, 6178.

[4] a) Z. Rao, P. Y. Tung, R. Xie, Y. Wei, H. Zhang, A. Ferrari, T. P. C. Klaver, F. Körmann, P. T. Sukumar, A. K. D. Silva, Y, C., Z. Li, D. Ponge, J. Neugebauer, O. Gutfleisch, S. Bauer, D. Raabe, *Science* **2024**, *2378*, 78; b) J. Li, J. Yu, Y. Zhang, C. Li, Y. Ma, H. Ge, N. Jian, L. Li, C. Y. Zhang, J. Y. Zhou, J. Arbiol, A. Cabot, *Adv. Funct. Mater.* **2025**, 2501485; c) C. Huang, J. Yu, C. Y. Zhang, Z. Cui, R. He, L. Yang, B. Nan, C. Li, X. Qi, X. Qi, J. Li, J. Y. Zhou, O. Usoltsev, L. Simonelli, J. Arbiol, Y. J. Lei, Q. Sun, G. Wang, A. Cabot, *Angew. Chem. Int. Ed.* **2025**, *64*, 202420488; d) H. Mollania, M. Oloomi-Buygi, A. Cabot, *J. Energy Storage* **2025**, *128*, 117023; e) C. Li, J. Yu, D. Yang, H. Li, Y. Cheng, Y. Ren, X. Bi, J. Ma, R. Zhao, Y. Zhou, J. Wang, C. Huang, J. Li, I. Pinto-Huguet, J. Arbiol, H. Zhang, S. Xin, A. Cabot, *J. Am. Chem. Soc.* **2025**, *147*, 8250; f) W. Bi, C. Li, D. Yang, Y.-Z. Zhang, L. Hu, Q. Gong, J. Zhang, Y. Zhang, M. Li, J. Wei, Y. Zhou, D. Zhou, T. Wu, L.-F. Chen, A. Cabot, *Energy Environ. Sci.* **2025**, *18*, 1929.

[5] C. Li, J. Yu, C. Zhang, D. Yang, J. Wang, H. Li, C. Huang, K. Xiao, Y. Cheng, Y. Ren, X. Qi, T. Yang, J. Li, J. Wang, G. Henkelman, J. Arbiol, J. Nan, A. Cabot, *J. Colloid. Interface Sci.* **2024**, *670*, 61.

[6] a) M. Du, P. Geng, C. Pei, X. Jiang, Y. Shan, W. Hu, L. Ni, H. Pang, *Angew. Chem. Int. Ed.* **2022**, *61*, 202209350; b) M. J. Theibault, C. R. McCormick, S. Lang, R. E. Schaak, H. D. Abruna, *ACS Nano* **2023**, *17*, 18402.

[7] a) Z. Du, C. Wu, Y. Chen, Q. Zhu, Y. Cui, H. Wang, Y. Zhang, X. Chen, J. Shang, B. Li, W. Chen, C. Liu, S. Yang, *Adv. Energy Mater.* **2021**, *12*, 2103228; b) F. Xing, J. Ma, K. I. Shimizu, S. Furukawa, *Nat. Commun.* **2022**, *13*, 5065; c) X. Han, G. Wu, S. Zhao, J. Guo, M. Yan, X. Hong, D. Wang, *Matter* **2023**, *6*, 1717; d) E. P. George, D. Raabe, R. O. Ritchie, *Nat. Rev. Mater.* **2019**, *4*, 515.

[8] a) R. He, L. Yang, Y. Zhang, X. Wang, S. Lee, T. Zhang, L. Li, Z. Liang, J. Chen, J. Li, A. Ostovari Moghaddam, J. Llorca, M. Ibáñez, J. Arbiol, Y. Xu, A. Cabot, *Energy Storage Mater.* **2023**, *58*, 287; b) R. He, L. Yang, Y. Zhang, D. Jiang, S. Lee, S. Horta, Z. Liang, X. Lu, A. Ostovari Moghaddam, J. Li, M. Ibanez, Y. Xu, Y. Zhou, A. Cabot, *Adv. Mater.* **2023**, *35*, 2303719.

[9] a) R. Guo, Y. Yang, C. Zhao, F. Huo, J. Xue, J. He, B. Sun, Z. Sun, H. K. Liu, S. X. Dou, *Adv. Funct. Mater.* **2023**, *34*, 2313168; b) H. Xu, R. Hu, Y. Zhang, H. Yan, Q. Zhu, J. Shang, S. Yang, B. Li, *Energy Storage Mater.* **2021**, *43*, 212.

[10] N. Liu, Z. Peng, J. Sun, Y. Tian, L. Mei, G. Lv, R. He, A. Cabot, J. Zhang, *Adv. Funct. Mater.* **2025**, *35*, 2419515.

[11] R. Gao, Y. Zhang, P. Chen, T. Yan, X. Gao, *Adv. Funct. Mater.* **2025**, 2502090.

[12] F. Han, Z. Wang, Q. Jin, L. Fan, K. Tao, L. Li, L. Shi, H. Q. Lu, Z. Zhang, J. Li, X. Zhang, L. Wu, *ACS Nano* **2024**, *18*, 15167.

[13] L. Yang, R. He, J. Chai, X. Qi, Q. Xue, X. Bi, J. Yu, Z. Sun, L. Xia, K. Wang, N. Kapuria, J. Li, A. Ostovari Moghaddam, A. Cabot, *Adv. Mater.* **2024**, 2412337.

[14] a) N. J. Orsini, B. Babić-Stojić, V. Spasojević, M. P. Calatayud, N. Cvjetićanin, G. F. Goya, *J. Magn. Magn. Mater.* **2018**, *449*, 286; b) Z. Fereshteh, M. Salavati-Niasari, *Adv. Colloid. Interface Sci.* **2017**, *243*, 86; c) K. Ahrenstorf, O. Albrecht, H. Heller, A. Kornowski, D. Gorlitz, H. Weller, *Small* **2007**, *3*, 271.

[15] a) C. T. Nguyen, T. M. Duong, M. Nguyen, Q. T. Nguyen, A. D. Nguyen, U. T. Dieu Thuy, Q. D. Truong, T. T. Nguyen, Q. L. Nguyen, P. D. Tran, *Int. J. Hydrogen Energy* **2019**, *44*, 13273; b) P. K. Sahoo, S. S. Kalyan Kamal, M. Premkumar, T. Jagadeesh Kumar, B. Sreedhar, A. K. Singh, S. K. Srivastava, K. Chandra Sekhar, *Int. J. Refract. Met. Hard Mater.* **2009**, *27*, 784.

[16] a) X. Huang, S. Tang, X. Mu, Y. Dai, G. Chen, Z. Zhou, F. Ruan, Z. Yang, N. Zheng, *Nat. Nanotechnol.* **2011**, *6*, 28; b) F. Lv, J. Feng, K. Wang, Z. Dou, W. Zhang, J. Zhou, C. Yang, M. Luo, Y. Yang, Y. Li, P. Gao, S. Guo, *ACS Cent. Sci.* **2018**, *4*, 1244; c) X. Yin, X. Liu, Y. T. Pan, K. A. Walsh, H. Yang, *Nano Lett.* **2014**, *14*, 7188.

[17] Y. Sun, X. Zhang, M. Luo, X. Chen, L. Wang, Y. Li, M. Li, Y. Qin, C. Li, N. Xu, G. Lu, P. Gao, S. Guo, *Adv. Mater.* **2018**, *30*, 1802136.

[18] X. Zhu, W. Zhao, Y. Song, Q. Li, F. Ding, J. Sun, L. Zhang, Z. Liu, *Adv. Energy Mater.* **2018**, *8*, 1800201.

[19] X. Tao, J. Wang, C. Liu, H. Wang, H. Yao, G. Zheng, Z. W. Seh, Q. Cai, W. Li, G. Zhou, C. Zu, Y. Cui, *Nat. Commun.* **2016**, *7*, 11203.

[20] a) J. Chen, E. Quattrocchi, F. Ciucci, Y. Chen, *Chem* **2023**, *9*, 2267; b) Y. Lu, C.-Z. Zhao, J.-Q. Huang, Q. Zhang, *Joule* **2022**, *6*, 1172; c) R. Soni, J. B. Robinson, P. R. Shearing, D. J. L. Brett, A. J. E. Rettie, T. S. Miller, *Energy Storage Mater.* **2022**, *51*, 97.

[21] a) C. Zhang, D. Li, Y. Wang, C. Shi, N. Wang, B. Chen, F. Ding, *Energy Fuels* **2023**, *37*, 18173; b) Y. Zhu, Z. Lao, M. Zhang, T. Hou, X. Xiao, Z. Piao, G. Lu, Z. Han, R. Gao, L. Nie, X. Wu, Y. Song, C. Ji, J. Wang, G. Zhou, *Nat. Commun.* **2024**, *15*, 3914.

[22] a) C. X. Bi, Y. J. Zhu, Z. Li, M. Zhao, X. Q. Zhang, B. Q. Li, J. Q. Huang, *Adv. Energy Mater.* **2024**, *14*, 2402609; b) B. Wang, L. Wang, B. Guo, Y. Kong, F. Wang, Z. Jing, G. Qu, M. Mamoor, D. Wang, X. He, L. Kong, L. Xu, *Adv. Mater.* **2024**, 2411725.

[23] X. Chen, L. Li, M. Liu, T. Huang, A. Yu, *J. Power Sources* **2021**, *496*, 229867.

[24] L. Liu, Y. Meng, Y. Ge, D. Xiao, *ACS Appl. Mater. Interfaces* **2023**, *15*, 33525.

[25] X. Wu, R. Xie, D. Cai, B. Fei, C. Zhang, Q. Chen, B. Sa, H. Zhan, *Adv. Funct. Mater.* **2024**, *34*, 2315012.

[26] D. Yang, Z. Liang, P. Tang, C. Zhang, M. Tang, Q. Li, J. J. Biendicho, J. Li, M. Heggen, R. E. Dunin-Borkowski, M. Xu, J. Llorca, J. Arbiol, J. R. Morante, S. L. Chou, A. Cabot, *Adv. Mater.* **2022**, *34*, 2108835.

[27] R. Liu, Z. Wei, L. Peng, L. Zhang, A. Zohar, R. Schoeppner, P. Wang, C. Wan, D. Zhu, H. Liu, Z. Wang, S. H. Tolbert, B. Dunn, Y. Huang, P. Sautet, X. Duan, *Nature* **2024**, *626*, 98.

[28] a) Y. Xu, W. Yuan, C. Geng, Z. Hu, Q. Li, Y. Zhao, X. Zhang, Z. Zhou, C. Yang, Q. H. Yang, *Adv. Sci.* **2024**, 2402497; b) B. Li, H. Wang, Y. Shen, Z. Zhang, Y. Xiong, M. Wang, W. Li, W. Zhou, J. He, *ACS Nano* **2025**, *19*, 12021; c) F. Han, L. Zhang, Q. Jin, X. Ma, Z. Zhang, Z. Sun, X. Zhang, L. Wu, *ACS Nano* **2025**, *19*, 9182; d) L. Chen, D. Wu, X. Li, Y. Li, G. Zu, S. Li, K. Li, J. Wang, *J. Mater. Chem. A* **2024**, *12*, 1765.